Journal of Fluids and Structures 82 (2018) 258–271

Contents lists available at ScienceDirect

Journal of Fluids and Structures

journal homepage: www.elsevier.com/locate/jfs

The pressure impulse of wave slamming on an oscillating wave energy converter

E. Renzi [a,*], Y. Wei [b], F. Dias [c]

[a] Department of Mathematical Sciences, Loughborough University, Loughborough, Leics LE11 3TU, UK
[b] Faculty of Science and Engineering, University of Groningen, Groningen, The Netherlands
[c] School of Mathematics and Statistics, University College Dublin, MaREI Centre, Belfield, Dublin 4, Ireland

ARTICLE INFO

Article history:
Received 26 February 2018
Received in revised form 28 June 2018
Accepted 6 July 2018
Available online 20 July 2018

ABSTRACT

Recent wave tank experiments on a flap-type wave energy converter showed the occurrence of extreme wave loads, corresponding to slamming events in highly energetic seas. In this paper, we analyse pressure-impulse values from available pressure measurements, for a series of experimental slamming tests. Then, we devise a pressure-impulse model of the slamming of a flapping plate, including the effects caused by air entrapment near the plate. Using a double conformal-mapping technique, we map the original domain into a semi-infinite channel, by means of Gauss' hypergeometric functions. This allows us to express the pressure impulse as a superimposition of orthogonal eigenfunctions in the transformed space. The mathematical model is validated against the experimental data. Parametric analysis shows that the system is much more sensitive to the impact angle than to the initial wetted portion of the flap. Furthermore, the presence of an aerated region determines the pressure-impulse values to increase significantly at all points on the flap surface.

1. Introduction

Slamming is the violent impact between a liquid surface and a structure (Faltinsen and Timokha, 2009; Dias and Ghidaglia, 2018). Traditionally, slamming has been studied and modelled in the context of seaplane mechanics and ship hydrodynamics. Slamming has been investigated also in the context of traditional and innovative breakwaters and offshore structures, see Oumeraci et al. (1993), Cuomo et al. (2010), Vicinanza et al. (2013) and Jose et al. (2016). Recently, experiments on a flap-type wave energy converter (WEC) showed the occurrence of slamming events in highly energetic seas, which are able to exert extreme loading on the device (Henry et al., 2014, 2015; Wei et al., 2016a).

Flap-type wave energy converters, such as the Oscillating Wave Surge Converter (OWSC), are among the most effective concepts to extract energy from the ocean (Babarit et al., 2012; Babarit, 2015). The OWSC is a pitching flap which works as an inverted pendulum, driven by the surge movement of waves in the nearshore (Renzi et al., 2014b). A power take-off mechanism (PTO) linked to the device enables transformation of kinetic energy into useful electricity. One of the most popular OWSC prototypes is the Oyster wave energy converter (WEC), which was able to generate up to 1 MWh in 5 h on a single power cylinder at the European Marine Energy Centre (EMEC) in Scotland (Renzi et al., 2014b). Wave slamming has indeed been observed on the Oyster 800 prototype at EMEC, when it was operating in a rough sea of significant wave height $H_s = 5$ m (Wei et al., 2016a). During extreme slamming events, the main engineering problem shifts from generating

* Corresponding author.
E-mail address: e.renzi@lboro.ac.uk (E. Renzi).

https://doi.org/10.1016/j.jfluidstructs.2018.07.007
0889-9746/

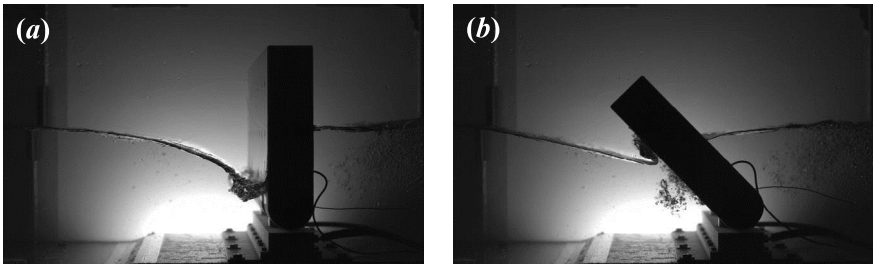

Fig. 1. Snapshots from the experiments of Wei et al. (2016a) at two different stages of a slamming event: (*a*) before slamming, the flap is vertical and the water line drops to its minimum level; (*b*) at impact the flap hits the water, creating a jet which is associated with a strong impulsive load on the structure. Waves are incoming from the left.

energy to ensuring device survival. Therefore, understanding the dynamics of flap slamming and calculating the maximum slamming loads is instrumental to inform the optimal design of OWSCs, thus increasing device reliability and reducing maintenance costs.

The slamming of an OWSC was first investigated by Henry et al. (2014) in three dimensions (3D). As the flap rotates seaward with high angular speed, it reaches a vertical position on encountering the wave trough. Then the waterline drops down the flap surface, and the flap violently hits the water, before the wave crest arrives. Later, Henry et al. (2015) and Wei et al. (2016a) performed additional experiments on a 2D model, using higher sampling rates that allowed more precise quantifications of the pressure peaks. Wei et al. (2016a) also devised a computational fluid dynamics (CFD) model, which successfully reproduced the main characteristics of the slamming event, such as flap angular speed and free-surface deformation. However, due to the very localised nature of the phenomenon and the stochastic behaviour of the experimental data, Wei et al. (2016a)'s CFD model could not capture the extreme pressure levels recorded in the experiments.

In this paper, we focus on the slamming pressure impulse, rather than on the peak pressure. Pressure impulse is defined as the integral of the pressure signal with respect to time, over the duration of the impact (Cooker and Peregrine, 1995; Faltinsen and Timokha, 2009). While slamming pressures usually have a stochastic behaviour, the pressure impulse is better behaved; therefore it is a better parameter to characterise extreme impacts (Lugni et al., 2006). This paper is organised as follows: First, we re-analyse all the experimental pressure recordings of Wei et al. (2016a) and use a local regression technique to calculate the mean curve. Then, we calculate the pressure impulse for all the experimental time series and the relevant regression data (Section 2). Second, we derive a pressure-impulse model of wave slamming on a plate, based on the seminal work of Cooker and Peregrine (1995) and Wood et al. (2000). The model includes the effect of air entrapment, which was neglected in the numerical study of Wei et al. (2016a), and is validated with the experimental data (Section 3). Finally, we perform a parametric analysis of the system, highlighting the contribution of the main engineering parameters (impact angle, contact point position, extent of the aerated region) on the maximum pressure impulse (Section 4). Our results show that the system is much more sensitive to the impact angle than to the initial wetted portion of the flap. Furthermore, in the presence of air trapping, the pressure impulse values increase significantly at all points on the flap surface.

2. Analysis of experimental data

2.1. Experimental layout

In order to develop a better understanding of the slamming of an OWSC, an experimental campaign was undertaken in the wave flume at Ecole Centrale de Marseille (ECM). The model OWSC was a 40th scale model with box-shape geometry (width $\times$ height $\times$ thickness $= 0.646$ m $\times$ 0.310 m $\times$ 0.0875 m), attached to a semi-circular tube under it, as shown in Fig. 1. The flap spanned the width of the wave flume, hence the experiment was two dimensional and represented a simplification of the slamming problem. A pressure sensor (Kistler 211B6, sampling rate 2000–6250 Hz) was installed at the centre of the flap near the mean water level, at a distance of 0.210 m above the hinge. In addition, a high speed camera (sample rates of 200 fps up to 2000 fps) was installed close to the glass wall of the flume, which could provide a superior view to capture images of the wave–OWSC interaction. More details about the experimental setup can be found in Henry et al. (2014).

A series of tests with various wave amplitudes A, wave periods T and water depths H were carried out in order to search for strong impacts. The case with the strongest impact was found for $A = 0.1$ m, $T = 1.9$ s and $H = 0.305$ m, with an average peak pressure of approximately 5 kPa. We emphasise that the wave conditions that resulted in strong impacts were sensitive to the distance between the wavemaker and the model OWSC, due to the re-reflection phenomenon occurring in the flume (Wei et al., 2016a).

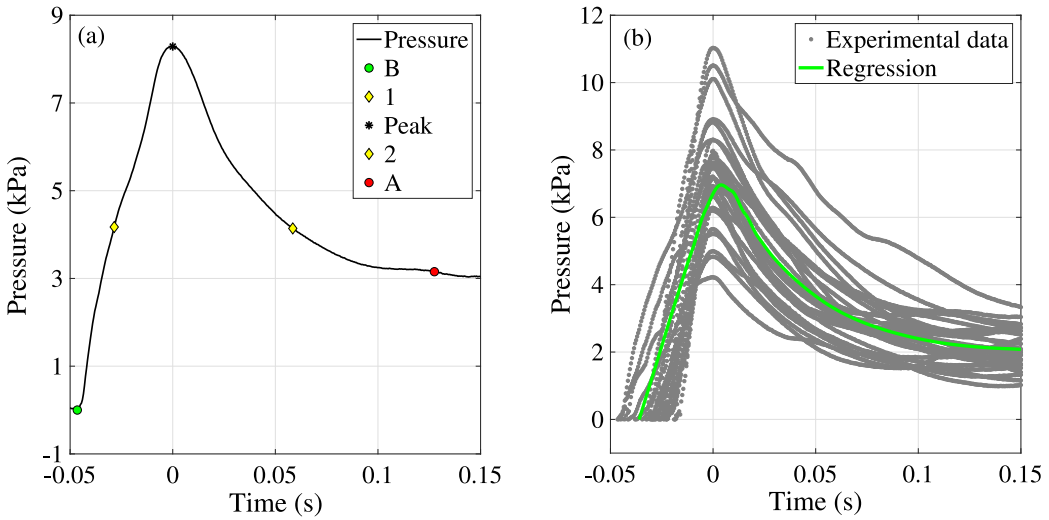

Fig. 2. (*a*) Plot of experimental pressure measurements for a typical impact (Wei et al., 2016a). The solid line represents the pressure data, the green dot (B) indicates the time t_b just before impact, the red dot (A) indicates the time t_a just after impact. The yellow parallelograms (1) and (2) indicate the instants at which the pressure is half the peak value and the star indicates the peak pressure. (*b*) Plot of the experimental pressure data for all the impacts analysed by Wei et al. (2016a). The green line shows the mean pressure curve obtained with a local regression technique. Note that the peak impulsive loads are followed by a quasi-hydrostatic phase of longer duration, but smaller intensity. (For interpretation of the references to colour in this figure legend, the reader is referred to the web version of this article.)

2.2. Experimental pressure time series

Fig. 2(*a*) shows the time series of the pressure recorded during a typical slamming event by Wei et al. (2016a). To display the full extent of the pressure jump, the pressure before impact is corrected as 0. The time axis is offset so that $t = 0$ corresponds to the pressure peak (starred marker). Note that the pressure plot shows a violent impact, followed by a quasi-hydrostatic phase of larger duration, but smaller intensity (Bullock et al., 2007).

The plot of Fig. 2(*a*) is similar to the records of pressure peaks generated by extreme waves impacting a wall, see for example Cooker and Peregrine (1995). Both phenomena (flap slamming, wave impact on a wall) belong to the same class of elementary loading process (ELP) in which there is run-up of liquid along a surface, see Dias and Ghidaglia (2018). In this type of ELPs, whose dynamics is predominantly incompressible, the hydrodynamic loads are generated by the change of fluid momentum. Such impacts are also characterised by unpredictable variations of the peak pressure. Fig. 2(*b*) shows a synoptic view of the pressure time series for 27 consecutive slamming events investigated by Wei et al. (2016a). In order to enhance the visual information contained in the scatter plot of Fig. 2(*b*), we applied a locally weighted regression technique to the experimental data (Cleveland, 1979). This technique produced the smoothed regression curve plotted in the same Fig. 2(*b*). The peak pressure of the regression is $p \sim 7$ kPa, whereas the scatter data values range from 4 kPa to about 11 kPa, exhibiting a strong stochastic behaviour. This is inherently linked to the extremely localised nature of the peaks, both in space and time. Such a nature makes it very difficult to model slamming events mathematically (Faltinsen and Timokha, 2009).

CFD programs are very successful in modelling OWSCs under normal operating conditions (Wei et al., 2013, 2015; Schmitt and Elsaesser, 2015; Abadie and Dias, 2016; Wei et al., 2016b; Dias et al., 2017). However, they can hardly be used to assess extreme slamming pressures. This is because their computational time is currently $O(10^4)$ longer than the real time, and also because of free-surface instabilities that are not well reproduced numerically (Dias and Ghidaglia, 2018). Wei et al. (2016a) performed numerical simulations of slamming on an OWSC using the commercial CFD package ANSYS FLUENT with a dynamic mesh method. Their numerical model was able to successfully reproduce the main characteristics of available experimental observations, such as flap motion and free-surface elevation. However, the numerical results underestimated the experimental peak pressure by a factor 10.

Analytical and semi-analytical theories have been used to model wave–OWSC interactions in linear and weakly nonlinear regimes (Renzi and Dias, 2012, 2013a, b; Renzi et al., 2014a; Sarkar et al., 2014; Michele et al., 2015; Noad and Porter, 2015; Sarkar et al., 2016; Michele et al., 2016, 2018). Such theories are normally applied when the flap rotation is small, about 10° from the vertical (Renzi and Dias, 2012). This excludes their applicability to slamming impacts, in which the flap rotation often reaches 60° with respect to the vertical (see again Fig. 1). Some success has been achieved in modelling slamming as an incompressible water entry problem. The latter was first investigated analytically in the seminal work of Wagner (1932). Using a potential flow model, Wagner (1932)'s solution gives the maximum pressure on a rigid wedge entering water:

$$p_{max} = \frac{1}{2}\,\rho\, u_{jr}^2,$$

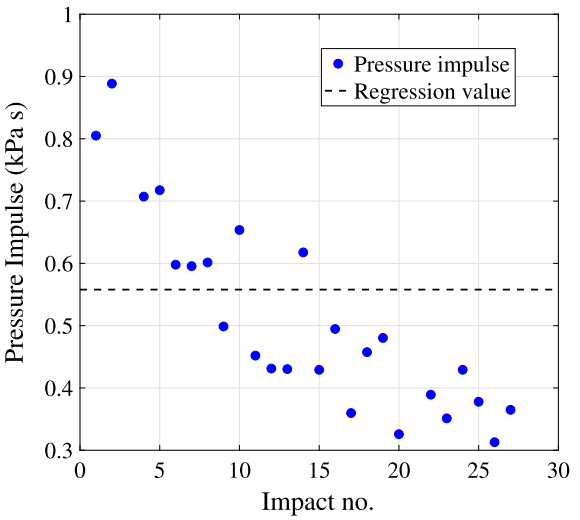

Fig. 3. Pressure-impulse values calculated from the 27 experimental pressure time series of Wei et al. (2016a). The dashed line represents the pressure impulse $P_r = 0.57$ kPa s obtained from the regression curve of Fig. 2(*b*).

where ρ is water density and u_{jr} is the jet root velocity. The latter can be calculated as a function of the wedge velocity and geometry (Dias and Ghidaglia, 2018). Henry et al. (2015) showed that Wagner's method gives a good estimate of the peak slamming pressure on a flap, although the theoretical values underestimate the experimental results. Several reasons might contribute to that mismatch: (i) the jet root velocity is normally very difficult to evaluate, (ii) the formation of air pockets near the contact point might influence the peak pressure values and (iii) flap slamming depends on specific parameters, such as initial water drop in front of the flap, flap angular velocity and impact angle, which cannot be easily related to the jet root velocity (Henry et al., 2015).

In summary, the peak pressures reached during a slamming event can be hardly modelled mathematically. Alternatively, pressure impulse is a better descriptor of wave slamming because: (i) it is more well-behaved than localised impact pressures, (ii) it can be determined analytically, based on the momentum and continuity equations for the fluid and (iii) it depends directly on impact angle and flap angular velocity. The latter can be obtained with a high degree of accuracy both with experimental measurements and CFD calculations, see Wei et al. (2016a). In the following, we will evaluate the pressure impulse for the experimental data of Fig. 2 (Section 2.3). Then we will use the new data to validate a pressure-impulse model of wave slamming on a flap (Section 3).

2.3. Pressure impulse

Pressure impulse is defined for a single slamming event as

$$P(\mathbf{x}) = \int_{t_b}^{t_a} p(\mathbf{x}, t)\,\mathrm{d}t, \tag{1}$$

where t_b and t_a are two representative times, respectively, before and after the event; p is pressure, $\mathbf{x}$ is the position vector on a Cartesian reference system and t is time. To calculate the pressure impulse from the experimental data, the representative time t_b before impact can be conveniently set as the time at which the pressure is minimum. This corresponds to the configuration in which the flap is almost vertical and the water level in front of it is lowest (see again Fig. 1). In the sample plot of Fig. 2(*a*), the time t_b is represented by a green circle. On the other hand, the representative time t_a after impact is more problematic to determine from the data, because the peak pressure is usually followed by an almost constant, quasi-hydrostatic pressure phase (see again Fig. 2*a*). This makes it difficult to exactly define the end of each impulsive loading process. We computed t_a assuming the linear relationship

$$t_a = t_b + 2(t_2 - t_1), \tag{2}$$

where t_1 and t_2 are the times at which the pressure is half the peak value, respectively, during the loading and unloading phases. In the sample plot of Fig. 2(*a*), t_1 and t_2 are represented by yellow diamonds and t_a by a red circle. Using the definition (2), t_a conveniently falls at the beginning of the quasi-hydrostatic phase that follows each impact, see for example Fig. 2(*a*). Once the characteristic times are defined for each experimental time series, use of Eq. (1) provides the relevant pressure impulse value at the sensor position.

Fig. 3 shows the pressure impulse P at the sensor position, for each of the 27 consecutive impacts recorded in the wave tank by Wei et al. (2016a), together with the regression value calculated using the mean pressure curve of Fig. 2(b). Interestingly, the plot of Fig. 3 reveals that the pressure impulse values, though distributed stochastically, decrease as the number of impacts increases, exhibiting a deterministic basis. This fact was not evident from the pressure recordings and is likely due to the re-reflection effects occurring in the wave tank. In their experiments, Wei et al. (2016a) documented the development of strong re-reflection by the paddle, which would contaminate the incident wave field. Such a phenomenon is inherently linked to the extreme nature of the wave–structure interaction occurring in slamming and can hardly be avoided. Wei et al. (2016a) showed that, as soon as the paddle was set into motion, the energy density of the incident wave would increase progressively towards a fully developed state. However, re-reflection effects would gradually break that balance, until the incident field was fully contaminated and its energy density changed, often decreasing. After several re-reflection cycles, a new balance was finally reached and the system set into a quasi-steady state. Therefore, higher energy levels at the beginning of the experiment might explain the initial pressure-impulse peaks in the plot of Fig. 3.

In the following section, we will derive a pressure-impulse model of flap slamming and will validate it against the experimental data.

3. Mathematical model

3.1. Governing equations

In this section, we develop a pressure-impulse model of slamming on an OWSC. The analysis is two dimensional and the effect of viscosity is unimportant (Wei et al., 2015). The typical impact speed of a slamming event in the experiments of Wei et al. (2016a) is about 1 m/s. Using Froude scaling with a full-to-model scale ratio $\lambda = 40$, the typical impact speed in full scale amounts to about $v_s = 6$ m/s, much less than the speed of sound in water $c = 1500$ m/s. That gives a Mach number $\mathrm{Ma} = v_s/c = 4 \times 10^{-3}$. If air is entrapped near the flap, the speed of sound in water can decrease down to 30 m/s, giving a Mach number $\mathrm{Ma} = 0.2$. In both cases, the Mach number gives $\mathrm{Ma}^2 < 0.1$, which means that water compressibility can be neglected (Dias and Ghidaglia, 2018). Conservation of mass then requires

$$\nabla \cdot \mathbf{u} = 0, \tag{3}$$

where $\mathbf{u}(x, y, t)$ is the velocity vector and $\nabla = (\partial/\partial x, \partial/\partial y)$; x and y, respectively, denote the horizontal and vertical coordinates, t is time. During a slamming event, fluid acceleration and the induced pressure gradient are usually much greater than convective and gravity accelerations, see Cooker and Peregrine (1995). Hence, the Euler equation simplifies to

$$\frac{\partial \mathbf{u}}{\partial t} = -\frac{1}{\rho}\nabla p, \tag{4}$$

where ρ is water density and $p(x, y, t)$ is pressure. Integration of Eq. (4) with respect to time and use of definition (1) give

$$\mathbf{u}_a - \mathbf{u}_b = -\frac{\nabla P}{\rho}, \tag{5}$$

where $\mathbf{u}_b$ and $\mathbf{u}_a$ define, respectively, the velocity field just before and after the impact. Furthermore, calculating the divergence of Eq. (5) and using conservation of mass (3) gives

$$\nabla^2 P = 0, \tag{6}$$

which shows that the pressure impulse is a harmonic function in the fluid domain. Note that the governing equation (6) has been derived without making any limiting assumptions on the wave amplitude and flap rotation.

Eqs. (5) and (6) define the pressure impulse model, which is now applied to the slamming problem described in Section 2. Fig. 4(a) and (b) show a typical slamming event on the seaward face of the flap. To simplify the choice of reference system in the mathematical model, we assume that the waves are incoming from the right. The total water depth away from the flap is H, which remains practically unchanged during the short time interval of the event (see again Fig. 1). Before impact, the flap is almost vertical (Wei et al., 2016a). Its wetted portion is denoted by μH, where the real parameter $\mu \in (0, 1)$, see Fig. 4(a). At the time of impact, the flap is inclined by an angle $\alpha \in (0, \pi/2]$ with respect to the horizontal x axis, see Fig. 4(b). The wetted portion roughly corresponds to the projection of the water depth H along the flap.

We now solve the governing equations (3)–(6) in the reference configuration at impact. Fig. 4(c) shows the relevant two dimensional boundary-value problem in an idealised trapezoidal domain. Since the pressure impulse is a local quantity, we only examine the seaward face of the flap, where the impact occurs and the maximum pressures are recorded. The origin of the reference system is located at the position of the hinge, which rests on the bottom of the ocean. The water depth is H, measured from the bottom $y = 0$ to the free surface $y = H$. The original wetted portion of the flap is described by $y = x \tan\alpha \in [0, \mu H \sin\alpha]$, whereas the wetted surface of the flap at impact is $y = x \tan\alpha \in [0, H]$. Note that the choice of an idealised free-surface profile of constant elevation (see again Fig. 4c) does not affect sensibly the model results, because the pressure impulse is only weakly dependent on the shape of the free boundary (Cooker and Peregrine, 1995).

The boundary conditions on the system are as follows:

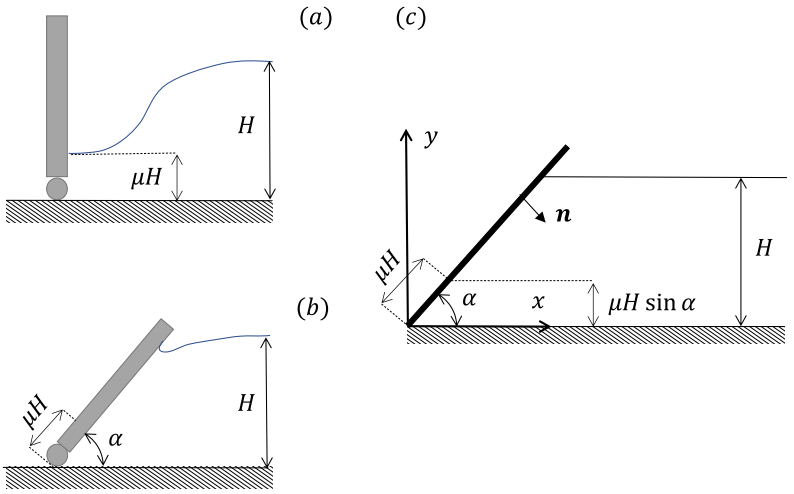

Fig. 4. Typical slamming event on the seaward side of a flap (waves are incoming from the right): (*a*) Sketch of the system before impact; (*b*) Sketch of the system at impact; (*c*) Idealised two-dimensional domain of trapezoidal shape where the boundary-value problem (6)–(12) is solved.

(i) On the free surface, the pressure is atmospheric and therefore constant. Without loss of generality, we choose this constant to be zero. Hence the pressure impulse (1) is

$$P = 0, \quad x \geq H \cot\alpha, \ y = H. \tag{7}$$

(ii) At the bottom, assumed impermeable, the normal component of the velocity is always $\mathbf{u} \cdot \mathbf{n} = 0$, where $\mathbf{n}$ is the local normal. Hence Eq. (5) gives

$$\frac{\partial P}{\partial y} = 0, \quad x > 0, \ y = 0. \tag{8}$$

(iii) On the flap, the normal is $\mathbf{n} = (\cos\alpha, -\sin\alpha)$. The dot product between Eq. (5) and $\mathbf{n}$ gives

$$(\mathbf{u}_a - \mathbf{u}_b) \cdot \mathbf{n} = -\frac{1}{\rho}\frac{\partial P}{\partial n}. \tag{9}$$

Now, on the portion of fluid in contact with the flap both before and after impact, we assume $\mathbf{u}_b \cdot \mathbf{n} \sim \mathbf{u}_a \cdot \mathbf{n}$. Indeed, experiments show that the velocity field of the portion of fluid which stays always in contact with the flap does not change much during the very short time interval $\Delta t = t_a - t_b \sim 0.1$ s, see Wei et al. (2016a). Experiments also show that the water velocity on the free surface in front of the flap before impact is close to zero, whereas the maximum speed of the flap at impact is much greater (about 3 m/s, see Wei et al., 2016a). Therefore, on the portion of fluid that becomes in contact with the flap during impact, we assume $\mathbf{u}_b \cdot \mathbf{n} \ll \mathbf{u}_a \cdot \mathbf{n} = U(y)$, where $U(y)$ is the normal component of the flap velocity at impact. As a result of these assumptions, Eq. (9) becomes

$$\frac{\partial P}{\partial n} = 0, \qquad x = y\cot\alpha, \ y \in [0, \mu H \sin\alpha), \tag{10}$$

$$\frac{\partial P}{\partial n} = -\rho U(y), \qquad x = y\cot\alpha, \ y \in [\mu H \sin\alpha, H]. \tag{11}$$

For a rotating motion with respect to the hinge, the normal velocity of the flap at impact is $U(y) = \omega y/\sin\alpha$, where ω is the angular speed in rad/s.

(iv) Finally, we request that the pressure impulse decays far away from the impact zone, so that

$$P(x, y) \to 0, \quad x \to \infty, \ y \in [0, H]. \tag{12}$$

Before moving to the solution of the boundary-value problem, we note that the geometrical layout of Fig. 4(*c*) is reminiscent of that used in the models of Wu (2007) and Mokrani (2012). Both authors analysed the impact of a triangular jet hitting a vertical solid wall with constant speed. The problem is conceptually equivalent to that of a vertical solid wall hitting an initially stationary liquid wedge. Wu (2007) used a potential-flow approach coupled with a numerical boundary element method, based on the hypotheses that the fluid is inviscid and incompressible and that the flow is irrotational. The numerical results were compared with those obtained with a similarity solution, in which the governing equations were converted into two integral equations and then linearised under a thin-jet assumption. This allowed (Wu, 2007) to find the surface profile of the liquid column and the pressure distribution on the vertical wall. Mokrani (2012) found a self-similar solution for the

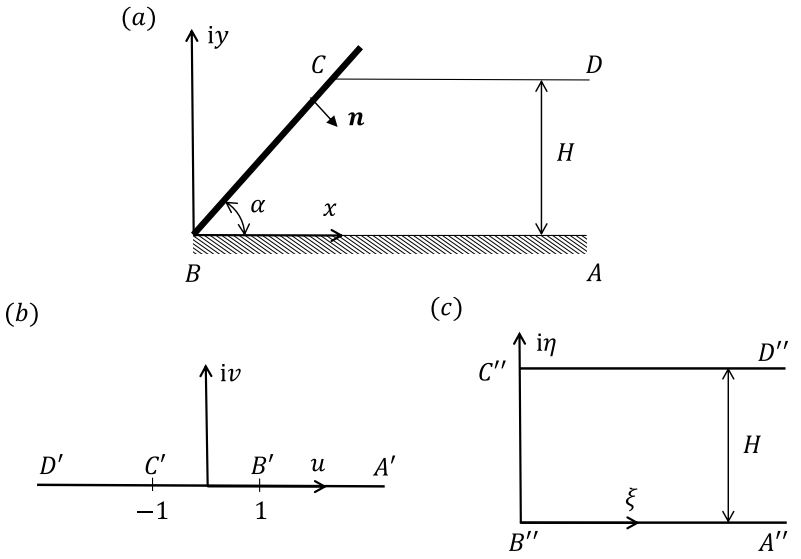

Fig. 5. Conformal mapping from (*a*) the original domain to (*b*) the $\tau = u + \mathrm{i}v$ plane and (*c*) the $\zeta = \xi + \mathrm{i}\eta$ plane.

same problem of a fluid wedge hitting a vertical wall at constant speed, and then determined the peak pressures on the wall. However, the models derived by Wu (2007) and Mokrani (2012) differ from the one studied in this paper, for the following reasons: (i) the boundary conditions of the two systems are different and are applied on different surfaces (see Mokrani, 2012, Chapter 6.2) and (ii) the present model is based on pressure impulse (see Eq. (1)) and takes into account the effect of air entrapment (see Section 3.4). Such elements were not investigated in the models of Wu (2007) and Mokrani (2012).

3.2. Conformal mapping

We now solve the governing equation (6) with the boundary conditions (7)–(12) by using a double conformal transformation in the complex plane. Referring to Fig. 5, we map the trapezoidal region $A - B - C - D$ into the upper half-plane $A' - B' - C' - D'$ with a Schwarz–Christoffel transformation, see Mei (1997) and Carrier et al. (2005). First, introduce the complex coordinate $z = x + \mathrm{i}y$, where i is the imaginary unit. Second, define the points $B = (0, 0)$, $C = (H \cot\alpha, H)$ and the points at infinity $A = \lim_{x\to\infty}(x, 0)$ and $D = \lim_{x\to\infty}(x, H)$. We now choose to map B and C, respectively, into $B' = (1, 0)$ and $C' = (-1, 0)$ in the τ plane, where $\tau = u + \mathrm{i}v$. As a consequence, A is mapped into $A' = \lim_{u\to\infty}(u, 0)$ and D into $D' = \lim_{u\to\infty}(-u, 0)$. The Schwarz–Christoffel transformation is then

$$z(\tau) = a \int_{\tau}^{1} \left(1 - \tau'\right)^{\alpha/\pi - 1} \left(1 + \tau'\right)^{-\alpha/\pi} \mathrm{d}\tau' + b, \tag{13}$$

where a and b are complex parameters to be determined (Carrier et al., 2005). The point B' at $\tau = 1$ corresponds to the point B at $z = 0$ (see again Fig. 5), so that $b = 0$. Similarly, the point C' at $\tau = -1$ corresponds to the point C at $z = H(\cot\alpha + \mathrm{i})$. Substituting the latter into Eq. (13) and evaluating the integral with formula 3.196 of Gradshteyn and Ryzhik (2007) gives

$$a = \frac{H(\cot\alpha + \mathrm{i})}{\mathrm{B}(\alpha/\pi, 1 - \alpha/\pi)}, \tag{14}$$

where $\mathrm{B}(x, y) = \Gamma(x)\,\Gamma(y)/\Gamma(x + y)$ is the Euler Beta function.

The complex integral in Eq. (13) does not admit a general analytical solution for all $\tau \in \mathbb{C}$ and for all $\alpha \in (0, \pi/2]$. However, if $\alpha = \pi/2$, then Eq. (13) simplifies to the well-known result

$$z = \frac{\mathrm{i}H}{\pi} \int_{\tau}^{1} \frac{\mathrm{d}\tau'}{\sqrt{1 - \tau'^2}} = \frac{H}{\pi} \mathrm{arccosh}(\tau), \tag{15}$$

where the principal branch for *arccosh*(τ) is chosen, such that $0 \le \arccos(u) \le \pi$ when $|u| \le 1$, see Gradshteyn and Ryzhik (2007); Olver et al. (2010).

Now let us transform the τ-plane into the semi-infinite channel $A'' - B'' - C'' - D''$ in the ζ-plane, where $\zeta = \xi + \mathrm{i}\eta$ (see Fig. 5). Using the previous result of Eq. (15), the Schwarz–Christoffel transformation is simply

$$\zeta(\tau) = \frac{H}{\pi} \mathrm{arccosh}(\tau). \tag{16}$$

With the double transform of Eqs. (13) and (16), the boundary-value problem of Eqs. (6) and (12) can be rewritten in the semi-infinite channel $A'' - B'' - C'' - D''$ as follows:

$$\frac{\partial^2 \bar{P}}{\partial \xi^2} + \frac{\partial^2 \bar{P}}{\partial \eta^2} = 0, \qquad \xi \in (0, \infty), \ \eta \in (0, H), \tag{17}$$

$$\bar{P} = 0, \qquad \eta = H, \tag{18}$$

$$\frac{\partial \bar{P}}{\partial \eta} = 0, \qquad \eta = 0, \tag{19}$$

$$\frac{\partial \bar{P}}{\partial \xi} = 0, \qquad \xi = 0, \ \eta \in [0, \bar{\mu} H), \tag{20}$$

$$\frac{\partial \bar{P}}{\partial \xi} = -\rho \bar{U}(\eta), \qquad \xi = 0, \ \eta \in [\bar{\mu} H, H], \tag{21}$$

$$\bar{P} \to 0, \qquad \xi \to \infty. \tag{22}$$

In the latter system of equations,

$$\bar{P}(\xi, \eta) = P(x(u(\xi, \eta), v(\xi, \eta)), y(u(\xi, \eta), v(\xi, \eta))), \tag{23}$$

while the point $(0, \bar{\mu} H)$ in the ζ-plane corresponds to the point $(0, \mu H \sin\alpha)$ in the z-plane. Finally, $\bar{U}(\eta) = U(y(\eta))$ corresponds to the transformation of $U(y)$ through Eqs. (13) and (16).

The equivalence between the systems (6)–(12) and (17)–(22) is granted by the fact that both $\tau(z)$ and $\zeta(\tau)$ are conformal transformations, see Carrier et al. (2005). As a consequence, at any point ζ in the region $A'' - B'' - C'' - D''$, the values of $\bar{P}$ (Eq. (23)) are equal to the values of P at the image point $z(\tau(\zeta))$ in the region $A - B - C - D$. Also, the outward normal at a point ζ_0 in the ζ-plane corresponds to the outward normal at $z_0 = z(\tau(\zeta_0))$ in the z-plane, which justifies the boundary conditions (19)–(21).

Before solving the boundary-value problem (b.v.p.) of Eqs. (17)–(22), we need to determine the parameter $\bar{\mu}$ and the function $\bar{U}(\eta)$ in the ζ-plane. Note that the flap is described by the segments $B - C$, $B' - C'$ and $B'' - C''$, respectively, in the z-, τ- and ζ-plane. For a point on the flap along $B' - C'$, Eq. (13) becomes

$$y = \frac{H}{\mathrm{B}(\alpha/\pi, \, 1 - \alpha/\pi)} \int_u^1 (1 - u')^{\alpha/\pi - 1} (u' + 1)^{-\alpha/\pi} \, \mathrm{d}u'. \tag{24}$$

Using the change of variable $\sigma = u' - u$ and formula 3.196 of Gradshteyn and Ryzhik (2007), the integral in (24) can be solved analytically, so that

$$y = \frac{\pi}{\alpha} \frac{H}{\mathrm{B}(\alpha/\pi, \, 1 - \alpha/\pi)} \left(\frac{1 - u}{1 + u} \right)^{\alpha/\pi} {}_2\mathrm{F}_1 \left(1, \frac{\alpha}{\pi}; 1 + \frac{\alpha}{\pi}; \frac{u - 1}{u + 1} \right), \tag{25}$$

where $y \in [0, H]$. In Eq. (25), ${}_2\mathrm{F}_1(a, b; c; Z)$ is the Gauss hypergeometric function, which is single-valued in the complex Z-plane with a branch-cut from 1 to $+\infty$ on the real axis, see Olver et al. (2010). Using formulae 15.4.20 and 15.8.1 of Olver et al. (2010), one can show that $\lim_{u \to -1} y = H$. Similarly, for a point on the flap along $B' - C'$, Eq. (16) becomes

$$\eta = \frac{H}{\pi} \arccos(u), \tag{26}$$

where $u \in [-1, 1]$. Hence, $\eta = \bar{\mu} H$ is the implicit solution of the system (25)–(26) when $y = \mu H \sin\alpha$. On the other hand, the flap normal speed in the transformed ζ-plane is

$$\bar{U}(\eta) = \frac{\omega}{\sin\alpha} y(\eta), \tag{27}$$

where $y(\eta)$ is the solution of the system (25)–(26) for given $\eta \in [\bar{\mu} H, H]$. Note that the transformation (25) cannot be inverted explicitly in terms of known functions. Therefore, the solution of (25)–(26) is parametric with respect to $u \in [-1, 1]$.

3.3. Solution

We are now ready to solve the b.v.p. (17)–(22). Separation of variables gives

$$\bar{P}(\xi, \eta) = \sum_{n=1}^{\infty} a_n \, \mathrm{e}^{-\lambda_n \xi / H} \cos\left(\lambda_n \frac{\eta}{H} \right), \tag{28}$$

which solves Eqs. (17)–(19) and Eq. (22). In Eq. (28), the λ_n's are the eigenvalues

$$\lambda_n = (2n - 1)\frac{\pi}{2}, \quad n = 1, 2, \ldots \tag{29}$$

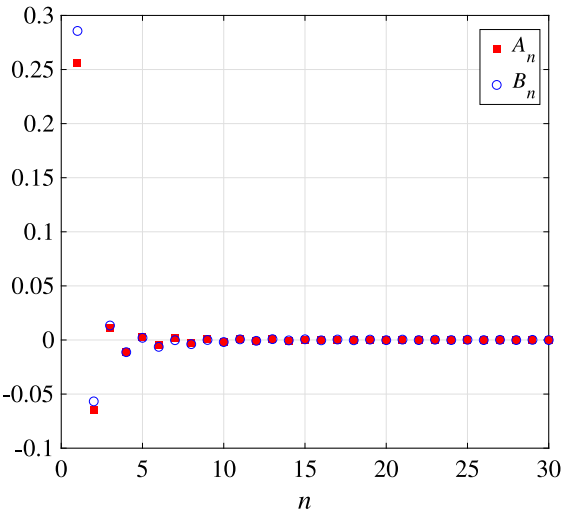

Fig. 6. Behaviour of the series coefficients A_n (32) and B_n (38). The system parameters are reported in Table 1.

Application of Eqs. (20)–(21) and use of the orthogonality property

$$\int_0^H \cos\left(\lambda_n \frac{\eta}{H}\right) \cos\left(\lambda_m \frac{\eta}{H}\right) \mathrm{d}\eta = \frac{H}{2}\delta_{nm}, \quad n, m = 1, 2, \ldots \tag{30}$$

where δ_{nm} is the Kronecker delta, gives then

$$\bar{P}(\xi, \eta) = \frac{2\rho\omega H^2}{\sin\alpha} \sum_{n=1}^{\infty} A_n \, \mathrm{e}^{-\lambda_n \xi/H} \cos\left(\lambda_n \frac{\eta}{H}\right). \tag{31}$$

In the latter,

$$A_n = \frac{1}{\lambda_n H^2} \int_{\tilde{\mu}H}^{H} y(\eta) \cos\left(\lambda_n \frac{\eta}{H}\right) \mathrm{d}\eta, \quad n = 1, 2, \ldots \tag{32}$$

are non-dimensional parameters and $y(\eta)$ is given by Eqs. (25)–(26). Numerical inspection of Eq. (32) for a typical flap configuration shows that the A_n's are fast-decaying functions of the modal order n, see Fig. 6. This ensures fast convergence of the series in Eq. (31) for $\xi \geq 0$. Finally, the solution in the original domain is obtained by substituting Eq. (31) into Eq. (23).

3.4. Effect of air entrapment

In this section we investigate the effect of air entrapment near the flap. The experimental data of Wei et al. (2016a) show that a semi-cylindrical region of water on the seaward side of the flap is aerated during the slamming phase, see Fig. 1(*a*). For a plunging breaker impacting on a wall, Wood et al. (2000) have shown that the presence of an air pocket near the wall causes the water to bounce back, thus increasing the pressure impulse on the structure. Similar dynamics can happen with flap slamming. When the flap hits the water, trapped air first contracts because of the impact, and then expands seaward, as the flap continues to pitch in the same direction. As a consequence, the fluid normal velocity after impact $\mathbf{u}_a \cdot \mathbf{n}$ increases with respect to the case in which no air is trapped. Following Wood et al. (2000), we assume that this increase of fluid velocity due to air entrapment is proportional to the flap speed $U(y)$ and is normal to the semi-circular profile of the air pocket. Referring to Fig. 7, the normal component of the velocity after impact in the aerated zone becomes $\mathbf{u}_a \cdot \mathbf{n} = U(y)[1 + f(y)]$, where

$$f(y) = \cos\left[\gamma\left(\frac{y}{H\sin\alpha} - \delta\right)\right] \tag{33}$$

is a semi-circular shape function. In Eq. (33), the parameters $\gamma = \pi/(\nu - \mu)$ and $\delta = (\nu + \mu)/2$ depend on the position of the bottom and top of the aerated region, respectively, $y_b = \mu H \sin\alpha$ and $y_t = \nu H \sin\alpha$, where $\nu \in (\mu, 1/\sin\alpha]$. Note that the bottom of the aerated region corresponds to the position of the contact point before impact. Wood et al. (2000) showed that a more complex analysis of air entrapment is not justified by the strongly stochastic nature of the impact properties that normally occur in experiments.

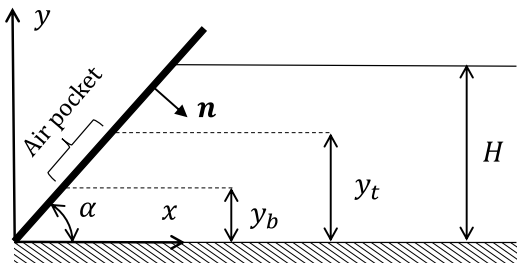

Fig. 7. Geometry of the system with air entrapment. The aerated region extends from $y_b = \mu H \sin\alpha$ to $y_t = \nu H \sin\alpha$.

The governing equation of the mathematical b.v.p. is still Eq. (6). However, the boundary conditions on the flap (10)–(11) are now replaced by

$$\frac{\partial P}{\partial n} = 0, \qquad x = y\cot\alpha, \ y \in [0, \mu H \sin\alpha), \tag{34}$$

$$\frac{\partial P}{\partial n} = -\rho U(y)[1 + f(y)], \qquad x = y\cot\alpha \ , y \in [\mu H \sin\alpha, \nu H \sin\alpha], \tag{35}$$

$$\frac{\partial P}{\partial n} = -\rho U(y), \qquad x = y\cot\alpha, \ y \in (\nu H \sin\alpha, H]. \tag{36}$$

The boundary condition on the free surface (7) and at the bottom (8) remain the same. The solution to this modified b.v.p. can be found by following the same steps as in Section 3.3. Using the double-conformal mapping from the z-plane to the ζ-plane and the method of separation of variables, the new expression for the pressure impulse in the transformed domain is

$$\bar{P}(\xi, \eta) = \frac{2\rho\omega H^2}{\sin\alpha} \sum_{n=1}^{\infty} B_n \, \mathrm{e}^{-\lambda_n \xi / H} \cos\left(\lambda_n \frac{\eta}{H}\right), \tag{37}$$

where

$$B_n = \frac{1}{\lambda_n H^2} \left\{ \int_{\bar{\mu} H}^{\bar{\nu} H} y(\eta)[1 + f(y(\eta))] \cos\left(\lambda_n \frac{\eta}{H}\right) \mathrm{d}\eta + \int_{\bar{\nu} H}^{H} y(\eta) \cos\left(\lambda_n \frac{\eta}{H}\right) \mathrm{d}\eta \right\} \tag{38}$$

and $\eta = \bar{\nu} H$ corresponds to $y = \nu H \sin\alpha$ via Eqs. (25)–(26). The B_n's are fast-decaying functions of the modal order n, as shown in Fig. 6. We shall now validate the pressure-impulse solution against the experimental data and study the sensitivity of the system on its main parameters.

4. Discussion

4.1. Experimental comparison

We consider a typical slamming event as described in Section 2. The parameters of the system representative of the experimental layout of Wei et al. (2016a) are summarised in Table 1. While the water depth, angular speed and impact angle can be determined directly from laboratory measurements, typical values for the wetting parameter μ and the air entrapment parameter ν have been determined by inspecting the frame sequences in Henry et al. (2014) and Wei et al. (2016a). Fig. 8 shows the profile of the pressure impulse on the flap, with respect to the vertical coordinate y, for the cases with and without air entrapment, respectively. A total of 30 normal modes were used to evaluate P in both cases. If air entrapment is neglected, the pressure impulse has a maximum of 0.44 kPa s slightly above the position of the sensor used in the experiments, and then it decreases down to a constant value in the initial contact zone. Air entrapment can amplify the pressure-impulse values at all points along the flap and shift the maximum inside the aerated zone. This is because aeration tends to increase the duration of the impact and to distribute high impulse values across a larger portion of the impacted surface, see Bullock et al. (2007). With air entrapment, the pressure impulse at the sensor position is 0.48 kPa s, whereas the maximum is 0.51 kPa s and is located at about 0.15 m from the bottom of the channel. Note that these values are consistent with the experimental data plotted in Fig. 3, except for the first stages where the system has not yet reached the quasi-steady state. In the next section we will perform a parametric analysis based on the pressure-impulse model to identify the role of the main physical quantities of the system.

Table 1
Parameters representing a typical slamming event in the experimental layout of Wei et al. (2016a).

Water depth H (m)	Angular speed ω (deg/s)	Impact angle α (deg)	Wetting parameter μ	Air pocket parameter ν
0.305	400	40	0.5	0.90

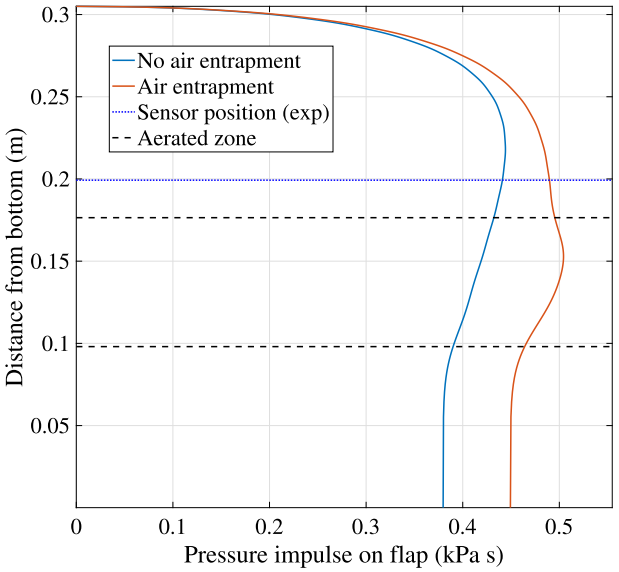

Fig. 8. Pressure impulse P (horizontal axis) versus distance from bottom y (vertical axis) for the parameters of Table 1. The values without air entrapment have been calculated with Eq. (31), those with air entrapment with Eq. (37).

4.2. Parametric analysis

In this section, we study the dependence of the system on the wetting parameter, impact angle and extent of the aerated region. First, we analyse the influence of the wetting parameter μ and impact angle α on the maximum pressure impulse on the flap, in the absence of air entrapment. Fig. 9 shows a contour plot of the maximum pressure impulse on the seaward face of the flap versus α and μ, in non-dimensional form. Note that the pressure impulse increases when the initial wetted area and the impact angle decrease. In particular, the contours show that the maximum pressure impulse is more sensitive to variations of the impact angle than of the initial wetted portion of the flap. The influence of the impact angle α on the pressure impulse is similar to the effect of the deadrise angle β on the impact pressure of a falling wedge. According to Wagner (1932)'s theory, the maximum impact pressure on the wedge depends on $\tan^{-2}\beta$, and so it increases as the deadrise angle tends to zero (Dias and Ghidaglia, 2018). A similar phenomenon occurs in the case of flap slamming, where the non-dimensional pressure impulse on the flap is maximum at small impact angles, which occur with strongly nonlinear oscillations of the flap.

Let us now analyse the influence of the air pocket dimension on the distribution of the pressure impulse along the flap. Fig. 10 shows the behaviour of the pressure impulse on the flap for several values of the air trapping parameter $\nu \in [\mu, 1/\sin\alpha]$, in non-dimensional form. Note that the presence of air trapping always amplifies the pressure impulse with respect to the case without air pockets. When the dimension of the aerated zone is small with respect to the full height of the flap, the pressure impulse increases only in an area inside the air pocket (see curve $\nu = 0.711$ of Fig. 10). However, when the dimensions of the air pocket are comparable to the flap height, the pressure impulse increases substantially at all points along the flap. In the extreme case where air entrapment occurs all along the flap, the maximum pressure impulse is almost twice as that without aeration (see curve $\nu = 1.556$ of Fig. 10). Interestingly, when no air is trapped the maximum pressure impulse is near the top of the flap. If a small air pocket appears near the bottom of the flap, then the maximum pressure impulse shifts towards that region. However, when the size of the air pocket increases, the maximum pressure impulse moves again towards the top of the flap (see Fig. 10). Therefore, the position of the maximum pressure impulse depends sensibly on the extent of the aerated region. A similar result was obtained by Bullock et al. (2007) when analysing experimental data of violent impacts on vertical walls.

From the non-dimensional pressure-impulse values of Fig. 10, an estimate of the slamming pressure can be obtained by assuming that the pressure time series is triangular (see again Fig. 2*a*). As a consequence, the peak pressure along the flap is approximately

$$p_{\max} \sim \frac{2\max\{P(y)\}}{\Delta t}\,, \tag{39}$$

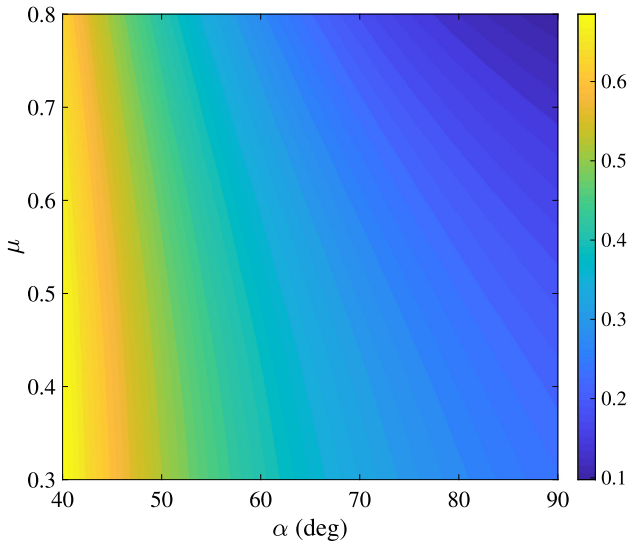

Fig. 9. Contour plot of the maximum pressure impulse on the seaward side of the flap, with respect to the wetting parameter μ and impact angle α, see again Fig. 4. Pressure impulse values are in non-dimensional form: $P/(\rho\omega H^2)$. Air entrapment is neglected.

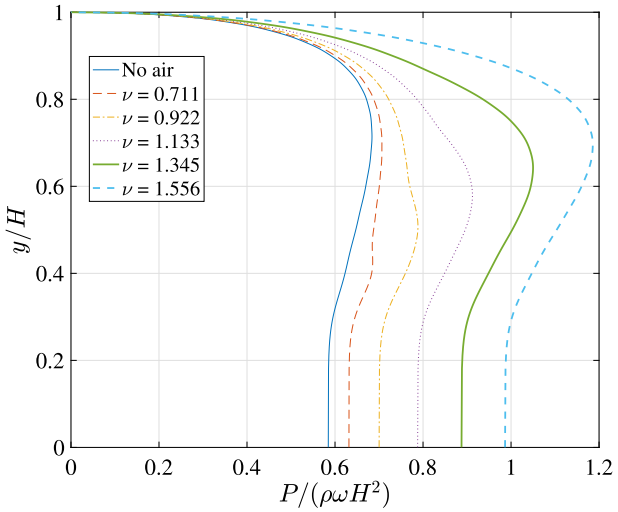

Fig. 10. Behaviour of the non-dimensional pressure impulse on the flap (horizontal axis) with respect to the non-dimensional distance from the bottom (vertical axis), for several values of the air pocket parameter ν. The other parameters are detailed in Table 1.

where Δt is the impact duration, see Cooker and Peregrine (1995). For the experimental tests of Wei et al. (2016a), the average impact duration is $\Delta t \sim 0.13$ s. Using the pressure-impulse values of Fig. 10 and the dimensional parameters of Table 1, the peak slamming pressure (Eq. (39)) falls in the interval

$$p_{\max} \in [6.8, 11.8] \text{ kPa}. \tag{40}$$

Such values agree very well with the experimental data shown in Fig. 2(*b*). However, there is evidence that the impact duration Δt tends to increase when air is trapped (Bullock et al., 2007). Therefore, a more accurate calculation of the peak pressure (39) from the pressure impulse in strongly aerated regimes would require a detailed knowledge of the correlation between the extent of the aerated zone and the impact duration, which necessitates further research.

5. Conclusions

We derived a pressure-impulse model of wave slamming on a flap-type wave energy converter. The mathematical model is based on a double conformal-mapping transform, which allows us to determine the pressure impulse on the seaward side

of the flap in terms of Gauss hypergeometric functions and Fourier series of orthogonal eigenfunctions in the transformed space. The initial pressure-impulse model was then extended to account for the effect of air entrapment near the surface of the flap, following a semi-empirical method devised by Wood et al. (2000). For the experimental layout of Wei et al. (2016a) described in Table 1, the mathematical model predicts a pressure-impulse value of around 0.48 kPa s at the sensor position. This value is very consistent with the experimental pressure-impulse values estimated from the pressure time series of Wei et al. (2016a). Parametric analysis also shows that the flap inclination (with respect to the vertical) at impact has a major effect on the pressure impulse: the larger the flap inclination at impact, the larger the maximum non-dimensional pressure impulse on the flap. The effect of the impact angle is therefore similar to that of the deadrise angle for a wedge entering calm water (Dias and Ghidaglia, 2018). Naturally, if the flap inclination with respect to the vertical becomes very large (i.e. the impact angle becomes very small), the device will be fully submerged. In that case, overtopping will occur and the dynamics will change considerably. The model also shows that the initial wetted area of the flap has a minor effect on the maximum pressure impulse. Finally, air entrapment is shown to have a major effect in enhancing the pressure-impulse values at all points along the flap and changing the position of the pressure-impulse peak. This might explain the failure of early attempts to evaluate the maximum impact pressure by means of CFD models that neglected the presence of air pockets near the surface of the flap.

The importance of air entrapment in enhancing the impact loads on the flap has been recently pointed out by Martinez Ferrer et al. (2016), who used the open-source CFD library OpenFOAM to model the same system studied in this paper. Martinez Ferrer et al. (2016) found that peak slamming pressures could only be captured when the manifestation of entrapped air was included in the CFD model. Our results confirm that slamming loads are enhanced by the formation of air bubbles trapped on the seaward side of the converter (see again Fig. 10). However, we note that Martinez Ferrer et al. (2016)'s CFD code presented several convergence issues when calculating the slamming torque at the hinge and the pressure peaks. Furthermore, such a high-end computational tool comes with a very expensive computational cost, needing about 12 days to model 60 s of physical time, on a quite advanced hardware architecture.

The present study offers a valuable analytical tool to obtain a reliable estimate of the peak pressure-impulse values at no computational cost. The analytical formulae presented in this paper are easy to implement in popular mathematical software packages (e.g. MATLAB®, see Palm, 2012) and can be evaluated in a matter of seconds. As such, they could be instrumental to hydrodynamicists and structural engineers designing flap-type devices, without the need of running very expensive computational models on supercomputers. Our results can be applied to identify a range of extreme cases that could then be studied more in depth with CFD models, thus optimising the design process while saving computational time.

6. Open questions

Our analysis points out some fundamental challenges in characterising slamming events for wave energy converters. First of all, experimental accuracy is paramount to obtain meaningful data for comparison with numerical and analytical models. A sampling rate of at least 1–10 kHz is necessary to characterise the impulsive pressure peak and relevant rise time in experiments, allowing one to fully reproduce the typical "church-roof" pressure diagram (see Bullock et al., 2007). At full scale, sampling rates of at least 20 kHz are recommended for global loading studies, and up to 100 kHz for local extreme loading analysis. This poses a fundamental challenge, because existing piezoelectric and piezoresistive pressure sensors can reach those very high natural frequencies only when used in air, not in water (Dias and Ghidaglia, 2018).

Second, the effects of scale ratio, impact dynamics, air compression and leakage still represent unsolved issues (Cuomo et al., 2010; Dias and Ghidaglia, 2018). In terms of scaling, it appears that pressure impulse is a more appropriate parameter to use than pressure, because the former can be scaled by Froude even when the latter cannot (Cuomo et al., 2010). Indeed, using Froude scaling may lead one to significantly overestimate the impact pressures at prototype scale. Therefore, appropriate correction factors for Froude scaling should be used when inferring the impact pressure from model data (Cuomo et al., 2010). Such factors exist for fixed structures, but have yet to be determined for moving bodies such as WECs. Recently, Dias and Ghidaglia (2018) have remarked that scaling remains the most important open problem for slamming applications, adding that surface tension effects, largely ignored until now, may play a more important role than originally thought.

Scale effects are also related to air compression, entrapment and leakage (Cuomo et al., 2010). Such dynamics still remain very elusive for fixed structures, not to mention moving devices. In this respect, future work should clarify the dynamics of air entrapment close to the surface of the prime mover, and the role of the compressibility of air/water mixture within the aerated region.

Acknowledgements

ER acknowledges fruitful discussions with Dr Mark Cooker. We are grateful to Dr Hideyasu Shimadzu for helping us with the statistical analysis of the experimental data and to the skilful student William Weller for his preliminary calculations. This study was partially supported by Science Foundation Ireland (SFI) under the research project "High-end Computational Modelling for Wave Energy Systems" (Grant SFI/10/IN.1/12996) in collaboration with Marine Renewable Energy Ireland (MaREI), the SFI Centre for Marine Renewable Energy Research (SFI/12/RC/2302).

References

Abadie, T., Dias, F., 2016. Numerical study of wave interaction with a modular oscillating wave surge converter. In: Proceedings of the Twenty-sixth International Offshore and Polar Engineering Conference, Rhodes, Greece, pp. 1021–1028.

Babarit, A., 2015. A database of capture width ratio of wave energy converters. Renew. Energy 80, 610–628.

Babarit, A., Hals, J., Muliawan, M., Kurniawan, A., Moan, T., Krokstad, J., 2012. Numerical benchmarking study of a selection of wave energy converters. Renew. Energy 41, 44–63.

Bullock, G.N., Obhrai, C., Peregrine, D.H., Bredmose, H., 2007. Violent breaking wave impacts. Part 1: Results from large-scale regular wave tests on vertical and sloping walls. Coast. Eng. 54, 602–617.

Carrier, G.F., Krook, M., Pearson, C.E., 2005. Functions of a Complex Variable. Society for Industrial and Applied Mathematics.

Cleveland, W.S., 1979. Robust locally weighted regression and smoothing scatterplots. J. Amer. Statist. Assoc. 74 (368), 829–836.

Cooker, M., Peregrine, D.H., 1995. Pressure-impulse theory for liquid impact problems. J. Fluid Mech. 297, 193–214.

Cuomo, G., Allsop, W., Takahashi, S., 2010. Scaling wave impact pressures on vertical walls. Coast. Eng. 57, 604–609.

Dias, F., Ghidaglia, J.-M., 2018. Slamming: Recent progress in the evaluation of impact pressures. Annu. Rev. Fluid Mech. 50, 243–273.

Dias, F., Renzi, E., Gallagher, S., Sarkar, D., Wei, Y., Abadie, T., Cummins, C., Rafiee, A., 2017. Analytical and computational modelling for wave energy systems: the example of oscillating wave surge converters. Acta Mech. Sinica 33 (4), 647–662.

Faltinsen, O.M., Timokha, A.M., 2009. Slamming. Cambridge University Press, USA.

Gradshteyn, I.S., Ryzhik, I.M., 2007. Tables of Integrals Series and Products. Academic Press, USA.

Henry, A., Abadie, T., Nicholson, J., McKinley, A., Kimmoun, O., Dias, F., 2015. The vertical distribution and evolution of slam pressure on an Oscillating Wave Surge Converter. In: Proceedings of the ASME 2015 34th International Conference on Ocean, Offshore and Arctic Engineering, OMAE2015. Newfoundland, Canada.

Henry, A., Rafiee, A., Schmitt, P., Dias, F., Whittaker, T., 2014. The characteristics of wave impacts on an oscillating wave surge converter. J. Ocean Wind Energy 1 (2), 101–110.

Jose, J., Podrazka, O., Obhrai, C., Gudmestad, O.T., Cieslikiewicz, W., 2016. Methods for analysing wave slamming loads on truss structures used in offshore wind applications based on experimental data. Int. J. Offshore Polar Eng. 26 (2), 100–108.

Lugni, C., Brocchini, M., Faltinsen, O.M., 2006. Wave impact loads: The role of the flip-through. Phys. Fluids 18, 122101.

Martinez Ferrer, P.J., Causon, D.M., Qian, L., Mingham, C.G., Ma, Z.H., 2016. Numerical simulation of wave slamming on a flap type oscillating wave energy device. In: Proceedings of the Twenty-sixth International Ocean and Polar Engineering Conference (ISOPE), Greece.

Mei, C.C., 1997. Mathematical Analysis in Engineering. Cambridge University Press.

Michele, S., Sammarco, P., d'Errico, M., 2016. Theory of the synchronous motion of an array of floating flap gates oscillating wave surge converter. Proc. R. Soc. Lond. Ser. A Math. Phys. Eng. Sci. 472, 20160174.

Michele, S., Sammarco, P., d'Errico, M., 2018. Weakly nonlinear theory for oscillating wave surge converters in a channel. J. Fluid Mech. 834, 55–91.

Michele, S., Sammarco, P., d'Errico, M., Renzi, E., Abdolali, A., Bellotti, G., Dias, F., 2015. Flap gate farm: From Venice lagoon defense to resonating wave energy production. Part 2: Synchronous response to incident waves in open sea. Appl. Ocean Res. 52, 43–61.

Mokrani, C., 2012. Impacts de vagues déferlantes sur un obstacle vertical. Modèle théorique et calcul numérique des pics de pression. (Ph.D. thesis), Université de Pau et des Pays de l'Adour, France.

Noad, I., Porter, R., 2015. Optimisation of arrays of flap-type oscillating wave surge converters. Appl. Ocean Res. 50, 237–253.

Olver, F.W.J., Lozier, D.W., Boisvert, R.F., Clark, C.W., 2010. NIST Handbook of Mathematical Functions. National Institute of Standards and Technology and Cambridge University Press.

Oumeraci, H., Klammer, P., Partenscky, H., 1993. Classification of breaking wave loads on vertical structures. J. Waterw. Port Coast. Ocean Eng. 119, 381–397.

Palm, W.J.III., 2012. Introduction To MATLAB® for Engineers. McGraw-Hill International Edition, Singapore.

Renzi, E., Abdolali, A., Bellotti, G., Dias, F., 2014a. Wave-power absorption from a finite array of Oscillating Wave Surge Converters. Renew. Energy 63, 55–68.

Renzi, E., Dias, F., 2012. Resonant behaviour of an oscillating wave energy converter in a channel. J. Fluid Mech. 701, 482–510.

Renzi, E., Dias, F., 2013a. Relations for a periodic array of oscillating wave energy converters. Appl. Ocean Res. 39, 31–39.

Renzi, E., Dias, F., 2013b. Hydrodynamics of the oscillating wave surge converter in the open ocean. Eur. J. Mech. B/Fluids 41, 1–10.

Renzi, E., Doherty, K., Henry, A., Dias, F., 2014b. How does Oyster work? The simple interpretation of Oyster mathematics. Eur. J. Mech. B Fluids 47, 124–131.

Sarkar, D., Doherty, K., Dias, F., 2016. The modular concept of the Oscillating Wave Surge Converter. Renew. Energy 85, 484–497.

Sarkar, D., Renzi, E., Dias, F., 2014. Wave farm modelling of Oscillating Wave Surge Converters. Proc. R. Soc. Lond. A 470, 20140118.

Schmitt, P., Elsaesser, B., 2015. On the use of Open Foam to model oscillating wave surge converters. Ocean Eng. 108, 98–104.

Vicinanza, D., Nørgaard, J.H., Contestabile, P., Andersen, T.L., 2013. Wave loadings acting on overtopping breakwater for energy conversion. J. Coast. Res. 65, 1669–1674.

Wagner, H., 1932. Über Stoß- und Gleitvorgänge and der Oberfläche von Flüssigkeiten. Z. Angew. Math. Mech. 12, 193–215.

Wei, Y., Abadie, T., Henry, A., Dias, F., 2016a. Wave interaction with an Oscillating Wave Surge Converter. Part II: Slamming. Ocean Eng. 113, 319–334.

Wei, Y., Abadie, T., Dias, F., 2016b. A cost-effective method for modelling wave-OWSC interaction. In: Proceedings of the Twenty-sixth International Offshore and Polar Engineering Conference, Rhodes, Greece, pp. 658–664.

Wei, Y., Rafiee, A., Elsaesser, B., Dias, F., 2013. Numerical simulation of an Oscillating Wave Surge Converter. In: Proceedings of the 32nd International Conference on Ocean, Offshore and Arctic Engineering, OMAE2013, Nantes, France.

Wei, Y., Rafiee, A., Henry, A., Dias, F., 2015. Wave interaction with an Oscillating Wave Surge Converter. Part I: Viscous effects. Ocean Eng. 104, 185–203.

Wood, D., Peregrine, D.H., Bruce, T., 2000. Wave impact on a wall using pressure-impulse theory. I: Trapped air. J. Waterw. Port Coast. Ocean Eng. 126 (4), 182–190.

Wu, G.X., 2007. Fluid impact on a solid boundary. J. Fluids Struct. 23, 755–765.